ACS Photonics

Article

pubs.acs.org/journal/apchd5

Highly Efficient and Tailorable On-Chip Metal−Insulator−Metal Plasmonic Nanofocusing Cavity

Zheng Li, Jun-long Kou, Myungki Kim, Jeong Oen Lee, and Hyuck Choo*

Department of Electrical Engineering, California Institute of Technology, Pasadena, California 91125, United States

Supporting Information

ABSTRACT: Simulation techniques were used to investigate the properties of a deep subwavelength-scale on-chip optical cavity composed of a highly efficient metal−insulator−metal 3D-tapered plasmonic nanofocusing waveguide and easily tailorable metal−insulator−metal plasmonic crystals. The configuration described here significantly enhanced the highly efficient field localization in the plasmonic nanofocusing waveguide at the center of the cavity due to the impedance tuning capabilities of the plasmonic crystals. The plasmonic crystals served as nanoscale input and output couplers with designable reflectivities and a clear band-stop regime around the telecommunication wavelength, λ_0 = 1.55 μm. Simulation studies indicated that this configuration could efficiently confine electromagnetic waves on the nanometer length scale through a field intensity enhancement of 7 × 10^3 and a Purcell enhancement of 8 × 10^3 within a volume of 1.4 × 10^{-5} λ_0^3. To evaluate the performance of the highly efficient metal−insulator−metal 3D-tapered plasmonic nanofocusing waveguide structure itself, the overall focusing efficiency, that is, the transmission rate from the wavelength-scale input side to the deep subwavelength-scale focusing core in the tapered waveguide, was calculated to be around 85%.

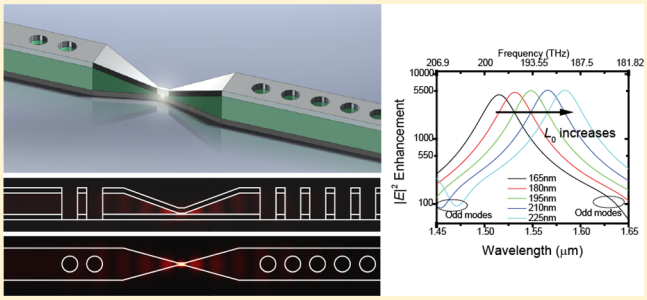

KEYWORDS: *on-chip nanophotonics, plasmonics, surface plasmon polaritons, nanoscale optical cavity, nanofocusing, tailorable nanoscale mirrors*

The efficient confinement and manipulation of light on the deep subwavelength scale are essential for enhancing the light−material interactions and improving the performance of nanophotonic devices. Surface plasmon polaritons (SPPs), which are free electron plasma oscillations coupled with electromagnetic waves that travel along a conductor−dielectric interface, have been investigated as a possible route to these functionalities.[1−4] Guided SPPs are tightly confined to the interface and are characterized by effective wavelengths that are ultrasmall compared to the vacuum wavelengths. SPPs enable the guidance, control, and confinement of light on the nanoscale, far below the diffraction limit. In view of these SPP properties, a variety of nanoscale devices and applications have been proposed, and some, including nanolasers, nanoscale light-emitting diodes (LEDs), nonclassical optical sources, and nanoscale detection and modulators, have been experimentally realized.[5−19] Among these devices, on-chip plasmonic devices are of particular interest for their utility in optoelectronic integrated circuits. These on-chip plasmonic devices are small in volume, consume low amounts of power, and provide good bandwidth modulation. The implementation of these nanoscale plasmonic devices requires the creation of highly efficient nanoscale plasmonic cavities. Researchers have theoretically and experimentally investigated a variety of nanoscale resonance mechanisms, including (but not limited to) nanoscale Fabry−Perot cavities, whispering gallery mode cavities, and plasmonic crystal (PLC) cavities.[20−37] Most of these nanocavity approaches were found to trade off the light coupling efficiency for the field enhancement. In this article, we propose an implementation of an on-chip nanoplasmonic cavity that can efficiently focus and confine light on the deep subwavelength scale as well as permit a relatively easy implementation of the optimized cavity-waveguide coupling rates in the design process.

The proposed cavity, which is shown in Figure 1, consists of two fundamental parts: (1) a tapered wave-guiding component with a highly efficient nanofocusing center and (2) tailorable nanoscale mirrors. The former is based on a recently demonstrated rectangular metal−insulator−metal (MIM) plasmonic nanofocusing waveguide that tapers three-dimensionally into a subwavelength-scale tip, namely, a three-dimensional nanoplasmonic photon compressor (3D NPC).[38] We create the wave-guiding component for the cavity by joining two 3D NPCs at their subwavelength tips. The tailorable nanoscale mirrors were formed from PLCs.[33] A PLC is a rectangular MIM waveguide with a periodic array of air holes oriented perpendicularly to the metal layers. PLCs behave similarly to photonic crystals. The number of air holes may be easily varied to adjust the reflectivity of the PLC

Received: March 27, 2014
Published: August 15, 2014

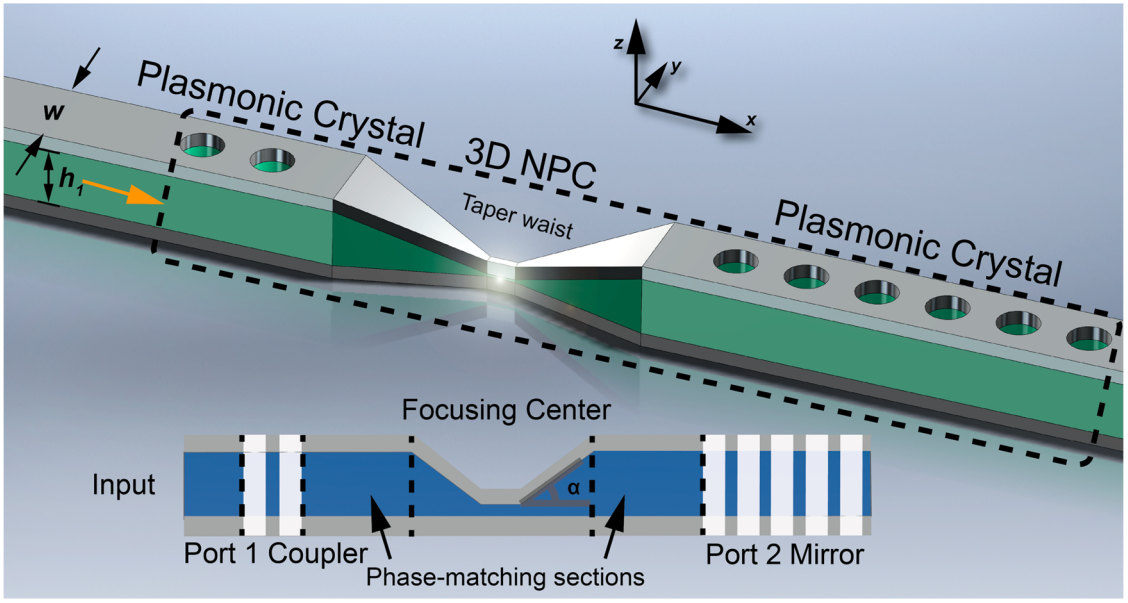

Figure 1. Schematic illustration of an optimized on-chip nanoscale plasmonic cavity: each individual part is illustrated in the cross-sectional view shown in the lower half of the figure. The dashed rectangular box indicates the cavity's volume.

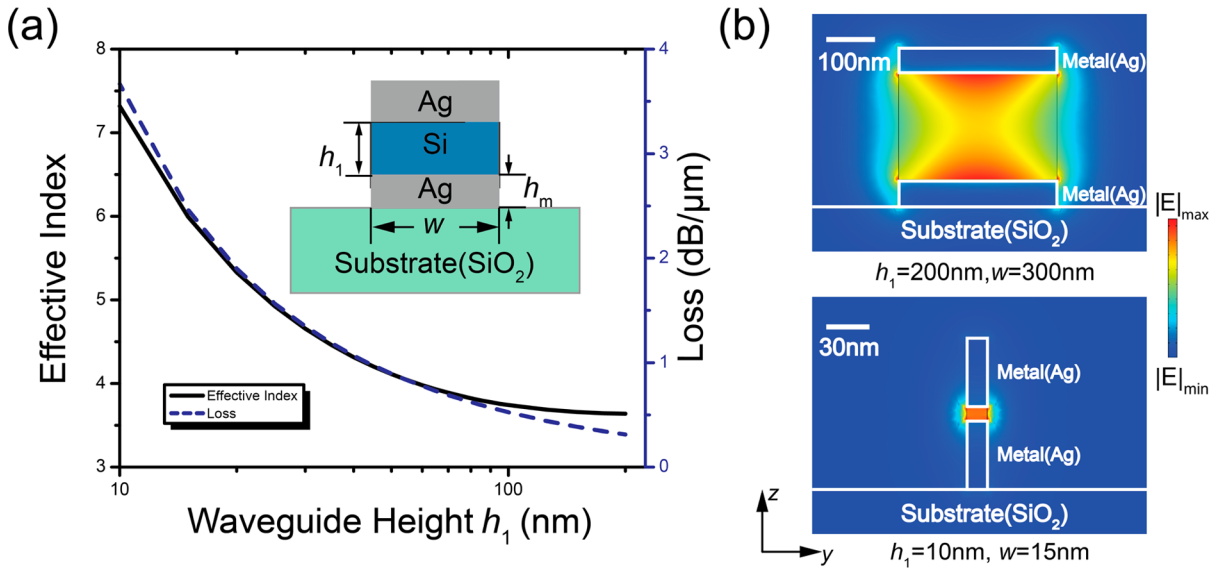

Figure 2. (a) Effective index and loss of the fundamental TM-like mode supported in the MIM waveguide, as a function of the height of the dielectric layer with h_1/w = 2:3 being constant. (b) Modal field amplitude profiles for dielectric layer dimensions of 200 nm × 300 nm or 10 nm × 15 nm. The metal thickness was held constant, h_m = 50 nm.

between 0% to almost 100%. This property of PLCs was used to adjust the coupling ratio between the cavity and the MIM waveguides connected to it. The 3D NPC and the PLC could be seamlessly integrated, as shown in Figure 1, because the devices shared the same MIM configuration. Our simulation studies suggested that an intensity enhancement of 7×10^3 and a mode volume of $1.4 \times 10^{-5}\ \lambda_0^3$ were achieved by employing a 3D NPC of high nanofocusing efficiency ($T_{eff} \sim 85\%$) and a pair of the optimized PLC mirrors. This configuration provides a simple method for designing highly efficient on-chip nanoscale plasmonic cavities capable of light coupling, focusing, and confinement in the deep subwavelength scale.

Compared to our previous device, which is a nanofocusing waveguide,[38] the proposed structure is a more complete, tailorable nanoscale optical resonant cavity made of two highly tailorable nanoscale mirrors formed by plasmonic crystals and the center waveguide section tapering down to the sub-10 nm scale. With strong field confinement and Purcell effect, the proposed device could greatly improve the device performances in a wide range of applications such as nanoLEDs, nano-modulators, and nanodetectors.[11−18] The MIM configuration with silicon as a dielectric layer also makes it easy to integrate the proposed structure with other on-chip nanophotonic devices. Most of all, the structure proposed in this manuscript shows the dramatically improved field intensity enhancement of over 7000 when its dielectric layer is 10 nm thick. In comparison, our previously reported device accomplishes the field enhancement of about 200 when the dielectric layer is 10 nm thick.

dx.doi.org/10.1021/ph500097m | ACS Photonics 2014, 1, 944−953

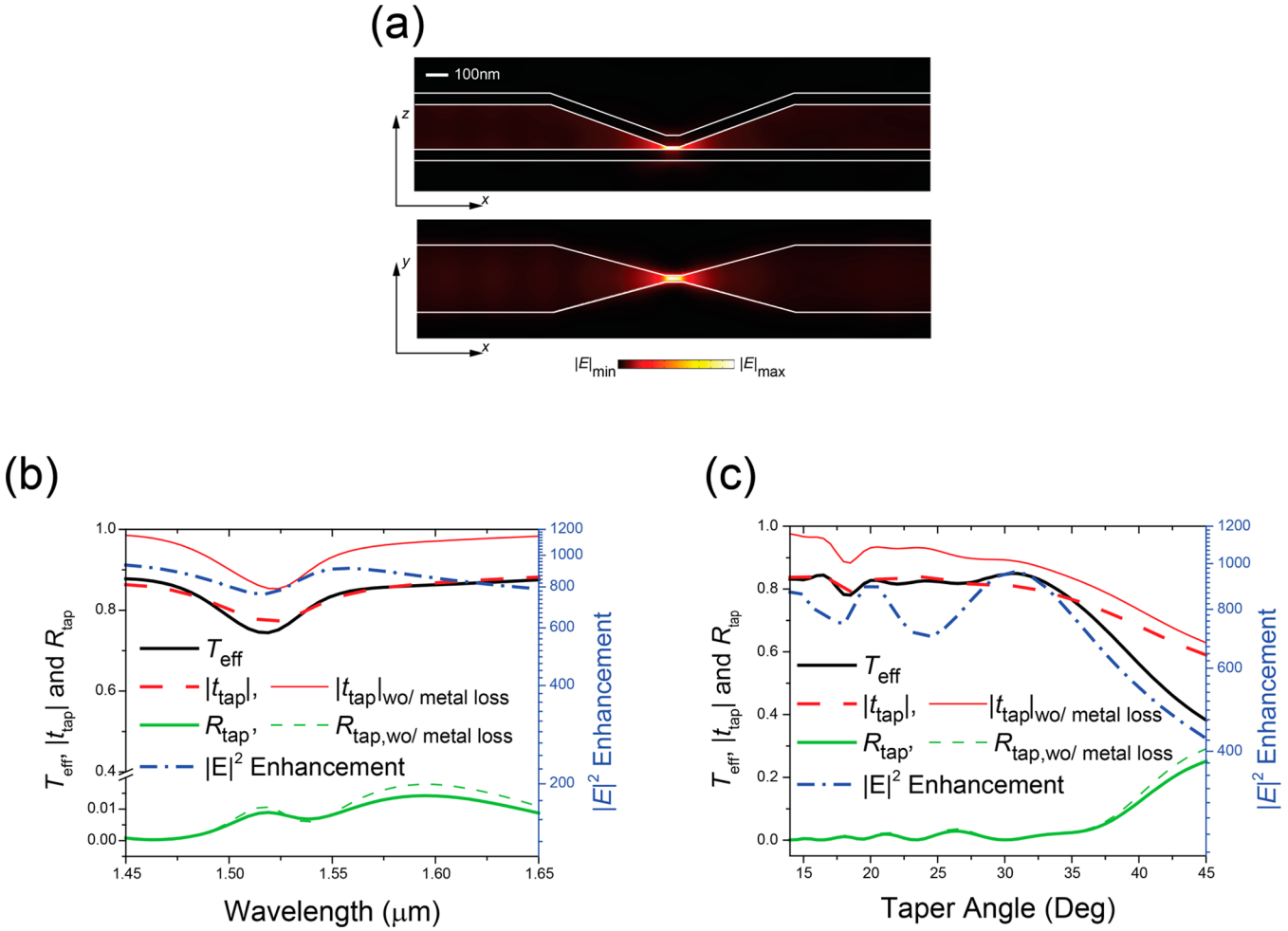

Figure 3. (a) Cross-sectional views of the electric field amplitude distribution in the *y*-plane (top) and the *z*-plane (bottom) along the center of the structure at λ_0 = 1.55 μm with a taper angle of α = 20° and a waist of L_w = 50 nm. Focusing efficiency, transmission ($|t_{tap}|$), and reflectance ($R_{tap} = |r_{tap}|^2$) with or without metallic loss, and field intensity enhancement (b) as a function of wavelength, for α fixed at 20°, and (c) as a function of the taper angle α, for λ_0 fixed at 1.55 μm.

RESULTS AND DISCUSSION

The proposed tailorable nanoscale plasmonic cavity is composed of two parts: (1) a three-dimensionally tapered MIM waveguide for deep subwavelength-scale nanofocusing and (2) highly configurable nanoscale mirrors prepared using MIM PLCs. The cavity is also connected to MIM waveguides in both sides for possible light coupling between the cavity and other on-chip integrated components.

Fundamental Component of the Platform: MIM Waveguide. Connected to either end of the cavity were MIM waveguides (as shown in Figure 1) with the dimensions h_1 = 200 nm and w = 300 nm. The supported fundamental mode of the waveguides was a TM-like mode (i.e., the majority of the electric field showed a TM orientation, perpendicular to the metal surfaces). Figure 2a presents the effective index and the loss of the fundamental TM-like mode as a function of the insulator height h_1 at the telecommunication wavelength λ_0 = 1.55 μm. Figure 2b shows the field profiles of the fundamental TM-like mode for h_1 = 200 and 10 nm. This fundamental mode did not exhibit a cutoff, even for waveguide dimensions of 10 nm. As the thickness of the dielectric layer was reduced, a waveguide height h_1 of less than 20 nm displayed an effective index as high as 7 and ensured that the electric field was strongly confined in the dielectric layer. This partially explained the strong nanoscale light-confining property of the proposed device.

Cavity Wave-Guiding Component: Tapered MIM Waveguide. Two of the 3D tapered highly efficient nanofocusing MIM structures described in our previous work were joined at the nanofocusing tips to form the central part of the cavity with a tapered waist (a device without air holes in Figure 1). The physical geometry of the assembled structure was similar to that of a Venturi tube, except that the MIM structures were linearly tapered from the end to the center. We also note that the height-to-width ratio (h_1/w) of the dielectric layer in the tapered section is kept constant at h_1/w = 2:3. The proposed structure could efficiently compress light from one side, focus it to the nanoscale hotspot in the structure's waist, and then decompress the light on the other side. Unlike the finite tip of a single-sided structure, the propagating mode in the positive x-direction traveled through the continuous smooth tapering and detapering geometry of the center section, producing approximately mode-matched conditions within a very short distance. These conditions minimized the energy loss due to reflection and scattering. In Figure 3a, hotspot formation was clearly observed at the center of the tapered waveguide whose dielectric height h_1 and the length of the waist L_w are 10 and 50 nm, respectively. The simulations were

dx.doi.org/10.1021/ph500097m | ACS Photonics 2014, 1, 944−953

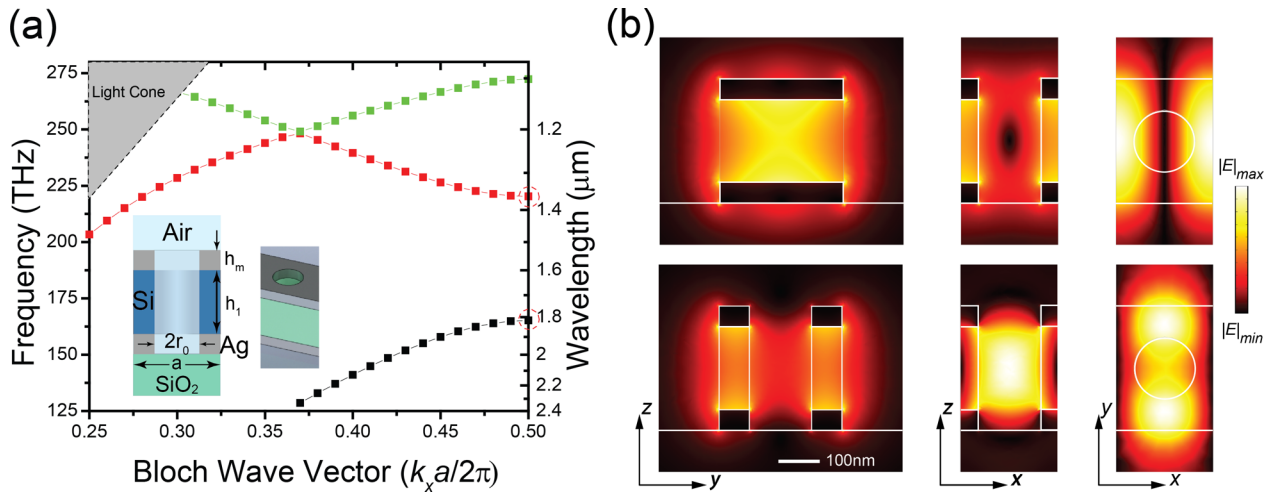

Figure 4. (a) Band diagram of the TM-like modes of the 1D PLC waveguide in the positive first Brillouin zone (inset: a cross-sectional view and a 3D illustration of a 1D MIM PLC unit cell). (b) Electric field amplitude profiles of the Bloch modes at $k_x = \pi/a$. The origin of the axes is assumed to be located at the center of the air hole. The three images in the upper row show the first-order mode along the $x = a/2$, $y = 0$, and $z = 0$ planes, from left to right, respectively. The other three images in the lower row show the second-order mode along the $x = 0$, $y = 0$, and $z = 0$ planes, from left to right, respectively.

conducted by injecting the fundamental mode into the left side of the structure, and both its reflection (r_{tap}; in amplitude) and transmission (t_{tap}; in amplitude) were calculated with respect to the beginning and ending positions of the tapered section.

As shown in Figure 3b, the structure exhibited a high nanofocusing efficiency T_{eff} and intensity enhancement $|E_{enh}|^2$ over a broad range of wavelengths. Between 1.45 and 1.65 μm, the intensity-enhancement factors remained between 750 and 950, and the focusing efficiency, T_{eff}, reached 85% for a taper angle α of 20°. The focusing efficiency T_{eff} was defined as the ratio of the power at the waveguide waist to the power measured at the beginning of the taper on the input port side. The field intensity enhancement was also similarly defined as the ratio of the field intensity averaged over the dielectric area of the tapered waist to the field intensity in the input port side when the fundamental mode was injected in the $+x$-direction. Although the linearly tapered structure functioned under the mode-matched conditions, the tapering and detapering processes applied to the traveling light generated multiple small reflections and produced a weak resonance, observed in the focusing efficiency and field-intensity enhancement, at $\lambda = 1.52$ μm, as shown in Figure 3b. Figure 3c shows that focusing efficiencies of 80−85% and field intensity enhancements of 700−950 could be achieved at $\lambda_0 = 1.55$ μm for α ranging between 14 and 30°. Both performance metrics began to drop significantly once the taper angle α had increased beyond 30°. The thickness of the dielectric layer of the MIM waveguides positioned before or after the taper is fixed; therefore, varying the taper angle altered the length of the taper section and, consequently, the length of the cavity. As a result, the $|E|^2$ enhancement plot shown in Figure 3c revealed multiple weak resonances. Our simulations indicated that the reflectance could be kept below 2.5% over the wavelength range of interest from 1.45 to 1.65 μm if the value of the taper angle was selected to fall below 30°.

The principal loss mechanism involved in the proposed approach was investigated by performing a series of simulations without metallic loss, so that only scattering and reflection losses were significant. These simulation results are presented in Figure 3b and c. Figure 3b shows that an optimal taper angle of 20° yielded nearly identical reflectance curves for the waveguides simulated with or without metallic loss, indicating that the reflected waves were directed exactly back toward the input port without significant second-order metallic absorption. The results also indicated that the device functioned under the small reflection condition and that the metallic and scattering losses appeared to dominate the loss mechanisms. We further compared the transmission ($|t_{tap}|$) with and without metallic loss to explore the dominant loss mechanism(s). A weak resonance dip was observed in both of those two curves at around 1.52 μm. Since it occurred even with the metallic loss being removed, we attributed the dip to the scattering loss at this particular wavelength range. As the wavelength of interest was moved away from the dip center, the transmission $|t_{tap}|$ without metallic loss approached 1 and the introduction of the metallic loss reduced the value to ~0.85. It suggested that the scattering loss was nearly zero and the metallic loss was dominant in the remaining frequency range of interest. Figure 3c shows that for $\alpha < 36°$, the reflectance $R_{tap} = |r_{tap}|^2$ reached below 3.5%. Regarding the metallic loss, as the taper angle was increased, the taper section was shortened, and the metallic loss became less. The corresponding value of the transmission $|t_{tap}|$ approached that obtained in the absence of the metallic loss. The transmission $|t_{tap}|$ calculated in the absence of metallic loss suggested that the scattering loss increased with the taper angle. These results were consistent with the adiabatic propagation assumption. Interestingly, the adiabatic focusing of a single mode into the sub-100 nm tapered waist section at the center of the cavity and the subsequent expansion of this mode past the waist toward the output port constituted compression and decompression processes characterized by a transmittance of the same value because the device is reciprocal and is symmetric about the center of its waist along the x-direction. As a result, the decompression efficiency approached T_{eff}, so that the total throughput power $|t_{tap}|^2$, which was equal to the product of the focusing efficiency T_{eff} and the decompression efficiency, became $|t_{tap}|^2 \approx T_{eff}^2$, especially for α less than 35° (Figure 3c). A taper angle exceeding 35°, caused T_{eff} to drop off more rapidly than $|t_{tap}|$, suggesting that the single-mode adiabatic propagation assumption was no longer valid. In this

dx.doi.org/10.1021/ph500097m | ACS Photonics 2014, 1, 944−953

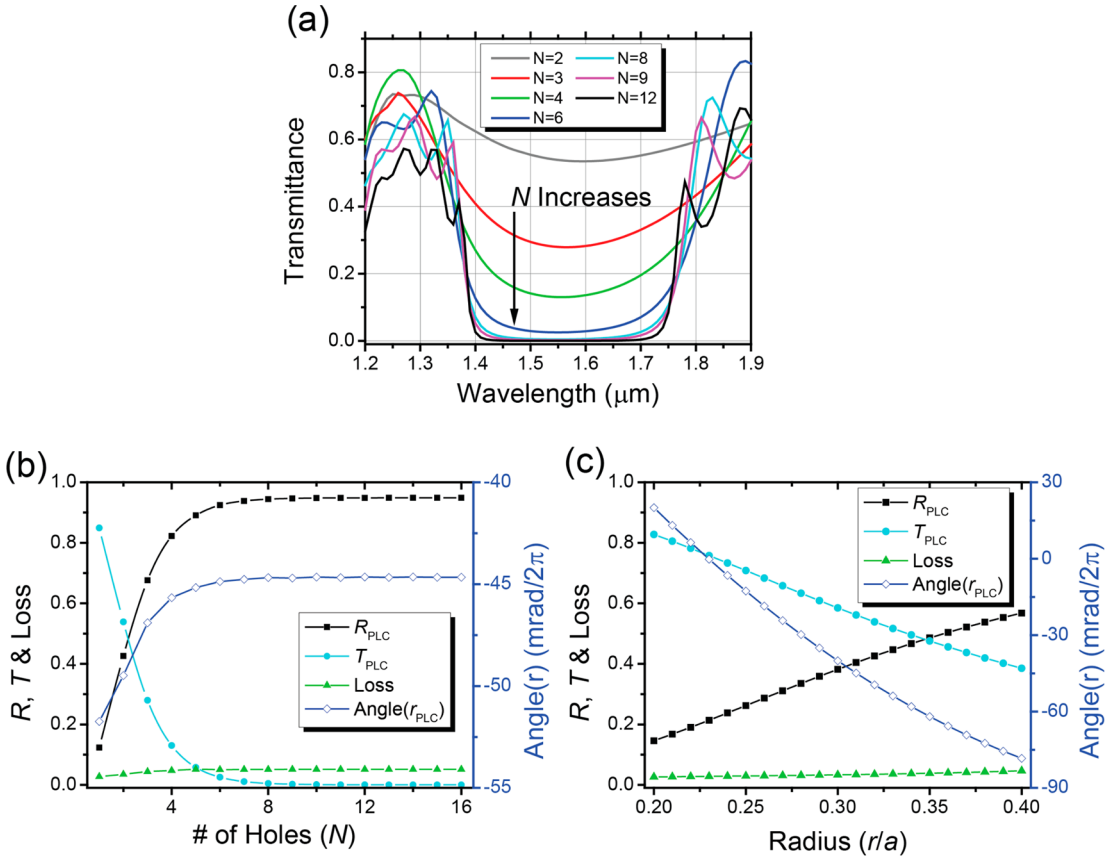

Figure 5. (a) Transmittance as a function of the TM-like fundamental mode in the PLC, over the range from 1.2 to 1.9 μm, for various air hole numbers N with r/a = 0.32. (b) The reflectance (R_{PLC}), transmittance (T_{PLC}), loss, and phase of the reflection (angle (r_{PLC})) of the fundamental TM-like mode as a function of the number of holes with r/a = 0.32. (c) R_{PLC}, T_{PLC}, loss, and angle (r_{PLC}) as a function of the air hole radius (r) in the PLCs with N = 2.

case, when the fundamental mode is injected, the abrupt reduction in the size of the MIM waveguide causes the excitation of higher-order modes in the tapered region and generated multimode transmission effects, in which a significant amount of energy flowed from the input to the output port via strong multimode excitation through very short, tapered sections.

Talorable Nanoscale Mirrors: MIM Plasmonic Crystals. The implementation of a highly efficient and useful nanoscale optical cavity requires the development of nanoscale cavity mirrors. To this end, we integrated MIM PLCs, which acted as tailorable mirrors, into the ends of the tapered nanoscale cavity center. The 1D PLC structure, whose unit cell configuration and 3D illustration are shown in the inset of Figure 4a, was composed of a periodic array of air holes formed along the MIM waveguide in the direction perpendicular to the metal layers.

The dimensions of the MIM waveguide used in the PLCs were the same as those of the MIM waveguides connected to the cavity: h_1 = 200 nm and w = 300 nm. The metal layer thickness was h_m = 50 nm. The periodicity and the radius parameters that characterized the hole array were selected to be a = 235 nm and r = 0.32a, respectively. In this section, we kept those values fixed unless we explicitly mentioned them. The band structure of the PLC for the TM-like polarization is shown in Figure 4a. The parameters a and r were adjusted to open a band gap between 1.36 and 1.81 μm. Figure 4b also shows the electric field amplitude |E| distributions of the Bloch modes of the lower and upper first bands located at the first Brillouin zone edge ($k_x = \pi/a$). The lower band mode exhibited a broad field distribution inside the high-index dielectric material and a field profile similar to the MIM fundamental TM mode in the y–z plane at $x = a/2$. The field of the upper band mode was mainly concentrated in the air hole region, and the cross-sectional distributions were highly modified by the presence of the air holes. All observations agreed generally with the theories developed to describe 1D photonic crystals.[39]

The dimensions of the MIM waveguide (h_1 = 200 nm and w = 300 nm) were carefully selected with consideration for the trade-offs among the loss of the fundamental mode, the cutoff condition for the second-order mode, and the challenges involved in nanoscale fabrication. The complete cutoff of the second-order mode (the second branch in the band structure at $k_x a/2\pi < 0.35$ touched the light-cone before it dropped to λ_0 = 1.55 μm) could only be guaranteed by further reducing the dimensions below the values selected here; however, such a reduction would have significantly increased the loss of the fundamental mode as well as posing nanofabrication challenges. Hence, the current dimensions were selected to introduce only a small loss in the fundamental mode while nearly achieving the second-order mode cutoff condition. At these dimensions, almost none of the energy in the second-order mode propagated through the structure or coupled into the fundamental mode due to both the sufficiently large effective index difference in the low-k_x region and to the modal orthogonality.

dx.doi.org/10.1021/ph500097m | ACS Photonics 2014, 1, 944–953

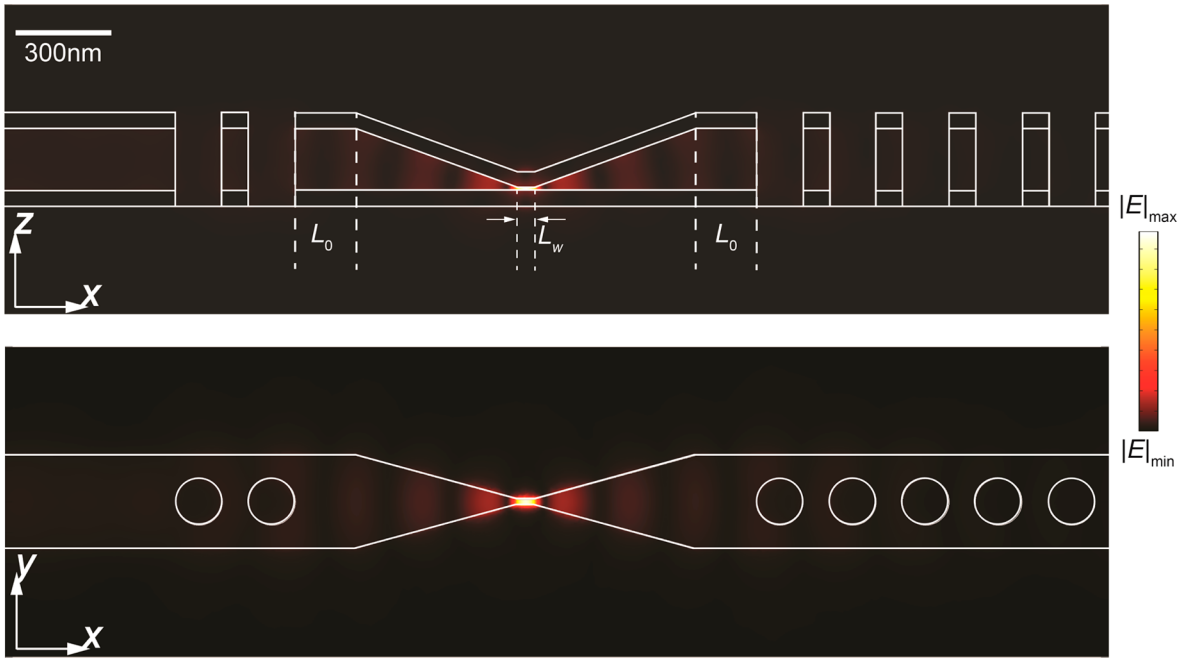

Figure 6. Electric field amplitude profiles in the *y*- and *z*-planes of the cavity at the resonance (λ_0 = 1.55 μm). The phase-matching conditions were accomplished by setting the taper angle α to 20°, the phase-matching section length L_0 to 195 nm, the waist length L_w to 50 nm, the periodicity a to 235 nm, and the air hole radius r to 0.32a.

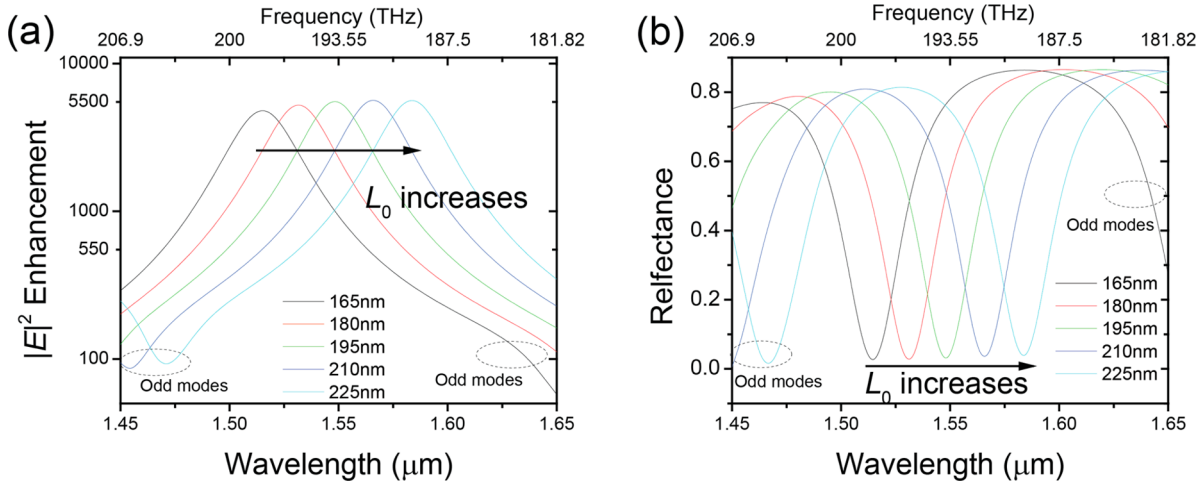

Figure 7. Frequency responses of (a) the electric field intensity enhancement and (b) the modal reflectance (taper angle α = 20°, taper waist length L_w = 50 nm, PLC periodicity a = 235 nm, hole radius r = 0.32a).

The number of air holes (N) could be varied to adjust the transmission rate of the fundamental mode between 1.41 and 1.72 μm, as shown in Figure 5a. These two transition rates were very close to the Bloch band-edge wavelengths observed in Figure 4a, and the results clearly agreed with the band gap analysis. For a fundamental mode of 1.55 μm, increasing N above 8 resulted in a reflectance (R_{PLC}) exceeding 94.9% (Figure 5b), and the metallic absorption and modal scattering losses fell below 5.1%. The selection of N values between 1 and 8 allowed us to adjust the reflectivity from 0.12 to 0.94. The air hole radius could also be varied to fine-tune the reflectance without increasing the loss: a 10% increase in the air hole radius linearly increased the reflectance by approximately 17%, as shown in Figure 5c. These two design parameters enabled the structural design of optimal nanocavity mirrors. It is worth noting that as N and r were increased, the intrinsic phase shift for the reflection only changed by a small degree (<5% of 2π), as indicated by the blue curve in Figure 5b and c. This feature further simplified the nanoscale resonator design process.

Integrated Nanoscale Optical Cavity with Strong Field Concentrated at the Center. The tapered MIM waveguide and MIM PLCs could be seamlessly connected to form an on-chip nanoscale optical cavity, as shown in Figure 1, without significantly reducing the device performance. The integrated device leveraged the strengths of each component and combined the components synergistically: the high nano-focusing capability of the tapered waveguide permitted a light compression at the deep subwavelength-scale region and the highly designable properties of the PLC mirrors permitted the in-and-out coupling ratios between the nanoscale optical cavity and the input and output ports to be optimized.

dx.doi.org/10.1021/ph500097m | ACS Photonics 2014, 1, 944−953

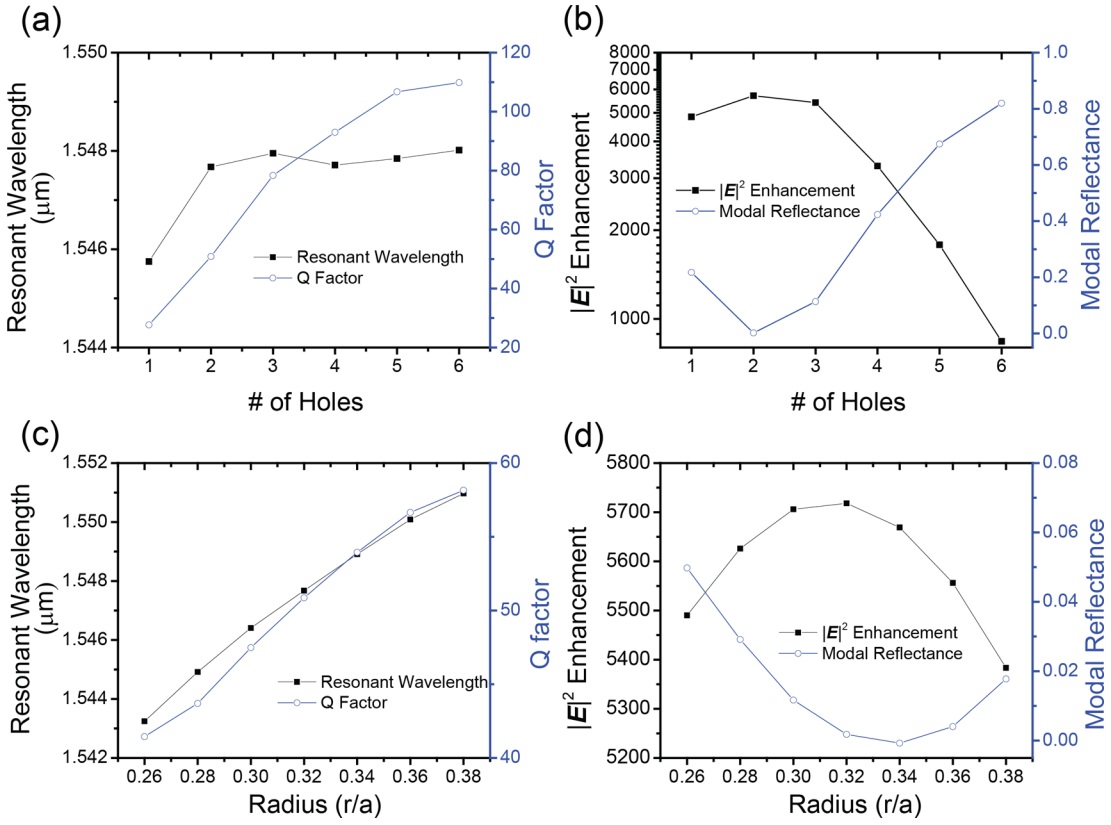

Figure 8. (a) Resonance wavelength and *Q*-factor as a function of the number of holes. (b) Field intensity enhancement and modal reflectance as a function of the number of holes. (c) Resonance wavelength and *Q*-factor as a function of r/a. (d) Field intensity enhancement and modal reflectance as a function of r/a. The optimal number of holes (N_1) and r/a were 2 and 0.32, respectively. The periodicity of the plasmonic crystal (a) was 235 nm. All points were obtained from the Lorentz fits to the original 3D simulation results.

The PLC on the input side needed a small number ($N \sim 2-3$) of air holes to form a semitransparent mirror that could adjust the light-coupling rate from the input port to the cavity. On the output side, the PLC contained a sufficient number of air holes ($N = 12$) to provide a strong reflection of around 95%. The sections of the MIM waveguide between the taper and the PLCs provided the phase compensation needed to properly engineer the resonance frequency of the cavity.

Before discussing the performance of the integrated device in the simulation studies, we will describe a simple yet highly useful design rule governing the length of the phase-matching MIM waveguide required to position the hot spot in the middle of the tapered waveguide, and to adjust the cavity resonance to the desired frequency. The geometry of the center tapered MIM waveguide was symmetric with respect to the major x-axis. It could, therefore, support even, odd, or hybrid modes, depending on the relative phases of the inputs on either side. The field enhancement at the center of the cavity could be maximized by ensuring that the inputs on either side were in-phase, thereby generating constructive interference at the center. The length L_0 of the phase-matching sections (shown in Figure 6) could thereby be designed to adjust the resonance frequency of the cavity (see the Supporting Information).

Figure 6 shows the field distribution for a taper angle of $\alpha = 20^\circ$ at the resonance wavelength $\lambda_0 = 1.55$ μm. A hot spot clearly formed at the center of the nanoscale cavity. A distinguishable standing wave pattern along the cavity indicated the cavity resonance, and the gradually varying intensity revealed the light compression–decompression procedure. On the output side, the field only visually penetrated around $N = 3$ or 4 air holes, suggesting that $N = 12$ for PLC was sufficient, in agreement with the R/T calculations presented in Figure 5.

The frequency responses of both the field intensity enhancements and the modal reflectance of the cavity were calculated as a function of the length L_0 of the phase matching region (Figure 7). At resonance, the field enhancement reached a maximum, the coupling rate between the input waveguide and the cavity was optimal, and the modal reflectance reached a minimum. As L_0 increased, the effective length of the total cavity increased and the resonance wavelength shifted to the red. The dips annotated by the dashed circles in Figure 7a,b correspond to the resonances of the odd modes that produced hotspots away from the cavity center. These odd modes were formed by waves that propagating with opposite signs as they entered the tapered center from opposite ends and led to destructive interference at the center. The effects of the odd modes significantly reduced the field enhancement below 100 or about one-ninth of the original value, 900.

The plots in Figure 7a,b illustrate that the length L_0 of the phase-matching sections could be adjusted to linearly change the resonance frequency within a small range without significantly changing the curve shape. In this context, the relationship between the length of the phase-matching sections and the resonance wavelength was accurately predicted by our simplified model (see the Supporting Information).

The PLC on the input side allowed us to adjust the energy coupling efficiency between the input and the cavity, thereby achieving near-zero modal reflectance or impedance-matched conditions. The optimal matching condition was found by

dx.doi.org/10.1021/ph500097m | ACS Photonics 2014, 1, 944–953

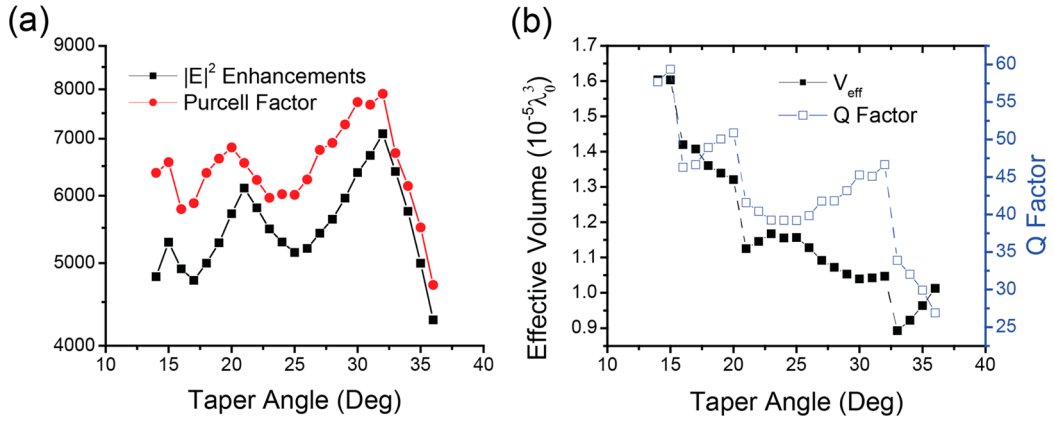

Figure 9. (a) Maximum field intensity enhancement and Purcell factor, both in logarithmic scale, as a function of the taper angle. (b) Effective volume and Q factor as a function of the taper angle (resonance wavelength: λ_0 = 1.55 μm).

varying N_1, which is the number of the air holes on the input-side PLC from 1 to 6. For large N_1 (>5), the PLC was highly reflective and provided good cavity confinement while significantly reducing the coupling rate from the input port into the cavity. As N_1 decreased, the coupling state between the input port and the cavity changed from an overcoupled to an under-coupled state, thereby lowering the field enhancement, as shown in Figure 8b. In the overcoupled region, N_1 was very small (≤1), and the PLC possessed a low reflectivity. These conditions permitted a large amount of energy to pass through the PLC into the cavity but also resulted in poor energy confinement inside the cavity or a leaky cavity on the input end. Consequently, the overcoupled region produced a low and broadband field enhancement (Figure 8b) indicated by a low Q-factor (Figure 8a). For N_1 equal to 2, the trade-off was balanced, and the optimal coupling conditions that resulted in a minimum modal reflection and maximum field enhancement were achieved. As mentioned in the previous section, the radius of the air holes r could be adjusted to provide even finer tuning of the coupling rate from the input-side PLC to the cavity and further optimize the performance of the device. The radius of the air hole r was varied from 0.26a to 0.38a, as shown in Figure 8c, which increased the Q-factor due to the large reflectance of the PLC. The resonance wavelength also became slightly red-shifted. The optimal matching condition was achieved for r equal to 0.32a.

In order to compare the cavity performances with respect to the taper angle, by keeping the same input-side PLC (N_1 = 2 and r = 0.32a), we designed the length of the phase-matching sections L_0 for each taper angle so that the cavity exhibited the hot spot in its center and resonated at ∼1.55 μm. The simulation results yielded $|E|^2$ as a function of the taper angle (between 14° and 36°), as presented in Figure 9. The value of $|E|^2$ varied between 5 × 10^3 and 7 × 10^3 and displayed peaks near 20° and 30°, reaching a maximum value of approximately 7 × 10^3 at 32°. The shape of the $|E|^2$ curve and the locations of the peaks were very similar to those of the intrinsic field intensity enhancement, as shown in Figure 3c. The Purcell enhancement factor closely followed $|E|^2$ and approached a maximum value of 8 × 10^3 for a taper angle of 32°. For all simulated cavities with different taper angles, the modal reflectance was kept below 5%. This value could be further reduced by fine-tuning the design of the input side PLC in each individual case.

Increasing the taper angle shortened the taper length. Hence, to ensure the cavity resonated at the same wavelength (or frequency) and exhibited the hot spot at its center, the length of the phase-matching section needs to be adjusted. For a shorter taper section, we needed longer phase-matching sections to provide the same effective optical path inside the cavity for the longitudinal mode of the same order. However, during the phase-matching designing procedure, the phase-matching sections themselves could become long enough to provide a phase delay φ_1 larger than 2π (longer than a half effective wavelength for the MIM waveguide), which is unnecessary. In this case, the phase-matching sections could be shortened until they only provided an equivalent phase delay below 2π (φ_1 − 2π). This design choice consequently reduced the order of the longitudinal mode, and its corresponding cavity volume for the given taper angle would be further minimized.

Hence, changing the taper angle from 14° to 36° resulted in the total phase delay larger than 6π. This implied the order of the corresponding longitudinal mode could be reduced by as larger as three. As a result, the Q-factor as well as the effective volume V_{eff} curves underwent three mode jumps as shown in Figure 9b. The reduction of the longitudinal mode order resulted in a sudden drop in both the Q factor and the effective volume V_{eff} due to a shorter light traveling time and a smaller cavity volume. Within the three continuous branches of the Q-factor and V_{eff} curves shown in Figure 9b, the longitudinal mode order was kept the same, and we observed that the Q-factor and V_{eff} showed opposite trends.

CONCLUSIONS

In this paper, we have discussed the design and simulated performance of an on-chip optimized nanoscale optical cavity. The proposed cavity was formed by seamlessly joining the highly efficient MIM plasmonic nanofocusing waveguide with a 3D-tapered waist and MIM plasmonic crystals to implement a highly efficient field-localizing nanoscale structure. The MIM PLCs, the properties of which could be adjusted simply by changing the air holes present, greatly enhanced the highly efficient nanofocusing capabilities of the 3D-tapered MIM plasmonic nanofocusing waveguide. Proper optimization of the coupling conditions between the MIM PLCs and the tapered waveguide whose focusing efficiency was 85% could achieve an intensity enhancement of 7 × 10^3 and a Purcell enhancement of 8 × 10^3 within a volume of 1.4 × 10^{-5} λ_0^3 in the proposed integrated structure. The proposed device could potentially

dx.doi.org/10.1021/ph500097m | ACS Photonics 2014, 1, 944−953

serve on-chip applications because of its strong and efficient nanoscale field enhancement and confinement that would lead to strong Purcell effect; its tailorable design that could be optimized for specific targets; its MIM waveguide geometry that makes it easy to be integrated with other on-chip photonic devices; and its practical fabrication approaches using thin film processes. With these desirable properties, the device could greatly assist in implementing a variety of on-chip applications including, but not limited to, cavity quantum electrodynamics (QED), nonlinear optics, and ultrafast nanoscale LEDs, modulators, and detectors.

METHODS

3D Simulations and Modal Solver. We used a commercial finite element method (FEM) software, the COMSOL Multiphysics RF Module, to perform full 3D frequency-domain simulations in the telecomm wavelength range (λ_0 = 1.55 μm). The optical indices of silicon and silica were n_{Si} = 3.5 and n_{SiO_2} = 1.45, respectively. The multi-coefficient models method hosted by Lumerical FDTD Solutions was used to fit the silver's optical constant measurements, which were reported by Johnson and Christine.[40] The waveguide modes were computed using the COMSOL Multiphysics RF Module.

Field Intensity Enhancement and Focusing Efficiency Definitions. The field intensity enhancement was calculated using the ratio of the average field intensities at the dielectric layers of the input and the waist center,

$$|E_{enh}(\omega)|^2 = \frac{\overline{|E_1(\omega)|^2}}{\overline{|E_0(\omega)|^2}} e^{2\alpha L_r}$$

where $\overline{|E_1(\omega)|^2}$ is the average field intensity measured at the waist center at the frequency ω and $\overline{|E_0(\omega)|^2}$ is a reference average field intensity measured at the input port, α is the loss factor of the fundamental TM-like mode of the MIM waveguide with a dielectric layer being 300 × 200 nm^2, and L_r is half of the tapered MIM waveguide length. This definition canceled out the variations in the injection efficiency of the MIM waveguide fundamental modes and accounted for the absorption of the fundamental mode propagating along the major axis. The focusing efficiency T_{eff} was defined as

$$T_{eff} = \frac{P_{dielectric}/\eta_0}{P_{input}}$$

where $P_{dielectric}$ is the power flowing into the dielectric layer at the taper waist center, P_{input} is the input power at the beginning of the taper, and η_0 is the ratio of the power flow in the dielectric layer to the total power flow in the fundamental mode. For this MIM waveguide, h_1 = 10 nm.

Transmission (t) and Reflection (r) Calculations. The transmission (t) and reflection (r) were calculated as scattering matrix parameters S_{21} and S_{11}, respectively, by introducing numerical port boundary conditions into the COMSOL Multiphysics RF Module.

Band Structure. The band structure and the corresponding Bloch modes were calculated in the COMSOL simulations of one unit cell of the PLC structure under Bloch boundary conditions applied in the x-direction.

Resonance Frequencies and Q Factors. The Q factors of the cavity modes were calculated according to $Q = f_0/\Delta f_0$, where f_0 is the resonance frequency of the mode and Δf_0 is the full width at half-maximum (fwhm) of the resonance peak in the intensity spectrum. It is worth noting that both the resonance frequency and the Q factor could be derived by fitting the frequency response curves of the field intensity enhancements and the input modal reflectance. We calculated both values and found them to be less than 1 nm and 5% for the resonance wavelengths and the Q factors, respectively.

Purcell Factor. The Purcell factor[41] was calculated according to

$$F_P = \frac{3}{4\pi^2}\left(\frac{\lambda_0}{n_{Si}}\right)^3 \frac{Q}{V_{eff}}$$

where λ_0 is the resonance frequency and V_{eff} is the effective mode volume of the cavity. The effective mode volume V_{eff} was defined as a function of the electrical energy density $W_E = 1/2(\partial(\varepsilon,\omega)/\partial\omega)\varepsilon_0|E|^2$ according to

$$V_{eff} = \frac{\int W_E dV}{\mathrm{avg}\{W_E\}}$$

where the numerator integrates the electrical energy density over the entire volume of the cavity and the denominator is the average of the central section of the taper waist.[42]

ASSOCIATED CONTENT

Supporting Information

Detailed descriptions of "Even mode injection conditions" (EMIC). This material is available free of charge via the Internet at http://pubs.acs.org.

AUTHOR INFORMATION

Corresponding Author

*E-mail: hchoo@caltech.edu.

Notes

The authors declare no competing financial interest.

ACKNOWLEDGMENTS

This work has been generously supported by the Powell Foundation Award (HC-1-616700) and the Rosen Bioengineering Center Endowment for Graduate Students (ENDOW.-ROSENBE).

REFERENCES

(1) Barnes, W. L.; Dereux, A.; Ebbesen, T. W. Surface Plasmon Subwavelength Optics. *Nature* **2003**, *424*, 824−830.

(2) Gramotnev, D. K.; Bozhevolnyi, S. I. Plasmonics beyond the Diffraction Limit. *Nat. Photonics* **2010**, *4*, 83−91.

(3) Schuller, J. A.; Barnard, E. S.; Cai, W.; Jun, Y. C.; White, J. S.; Brongersma, M. L. Plasmonics for Extreme Light Concentration and Manipulation. *Nat. Mater.* **2010**, *9*, 193−204.

(4) Kim, K. Y. *Plasmonics−Principles and Applications*; InTech: Rijeka, Croatia, 2012.

(5) Hill, M. T.; Oei, Y.-S.; Smalbrugge, B.; Zhu, Y.; Vries, T. d.; Veldhoven, P. J. v.; Otten, F. W. M. v.; Eijkemans, T. J.; Turkiewicz, J. P.; Waardt, H. d. Lasing in Metallic-Coated Nanocavities. *Nat. Photonics* **2007**, *1*, 589−594.

(6) Seo, M.-K.; Kwon, S.-H.; Ee, H.-S.; Park, H.-G. Full Three-Dimensional Subwavelength High-Q Surface-Plasmon-Polariton Cavity. *Nano Lett.* **2009**, *9*, 4078−4082.

(7) Nezhad, M. P.; Simic, A.; Bondarenko, O.; Slutsky, B.; Mizrahi, A.; Feng, L.; Lomakin, V.; Fainman, Y. Room-Temperature

Subwavelength Metallo-Dielectric Lasers. *Nat. Photonics* **2010**, *4*, 395−399.
(8) Kwon, S.-H.; Kang, J.-H.; Seassal, C.; Kim, S.-K.; Regreny, P.; Lee, Y.-H.; Lieber, C. M.; Park, H.-G. Subwavelength Plasmonic Lasing from a Semiconductor Nanodisk with Silver Nanopan Cavity. *Nano Lett.* **2010**, *10*, 3679−3683.
(9) Khajavikhan, M.; Simic, A.; Katz, M.; Lee, J. H.; Slutsky, B.; Mizrahi, A.; Lomakin, V.; Fainman, Y. Thresholdless Nanoscale Coaxial Lasers. *Nature* **2012**, *482*, 204−207.
(10) Kim, M.-k.; Li, Z.; Huang, K.; Going, R.; Wu, M. C.; Choo, H. Engineering of Metal-Clad Optical Nanocavity to Optimize Coupling with Integrated Waveguides. *Opt. Express* **2013**, *21*, 25796−25804.
(11) Okamoto, K.; Niki, I.; Shvartser, A.; Narukawa, Y.; Mukai, T.; Scherer, A. Surface-Plasmon- Enhanced Light Emitters Based on InGaN Quantum Wells. *Nat. Mater.* **2004**, *3*, 601−605.
(12) Anger, P.; Bharadwaj, P.; Novotny, L. Enhancement and Quenching of Single-Molecule Fluorescence. *Phys. Rev. Lett.* **2006**, *96*, 113002.
(13) Taminiau, T. H.; Stefani, F. D.; Segerink, F. B.; Hulst, N. F. v. Optical Antennas Direct Single-Molecule Emission. *Nat. Photonics* **2008**, *2*, 234−237.
(14) Maksymov, I. S.; Besbes, M.; Hugonin, J. P.; Yang, J.; Beveratos, A.; Sagnes, I.; Robert- Philip, I.; Lalanne, P. Metal-Coated Nanocylinder Cavity for Broadband Nonclassical Light Emission. *Phys. Rev. Lett.* **2010**, *105*, 180502.
(15) Choy, J. T.; Hausmann, B. J. M.; Babinec, T. M.; Bulu, I.; Khan, M.; Maletinsky, P.; Ya- coby, A.; Loncar, M. Enhanced Single-Photon Emission from a Diamond-Silver Aperture. *Nat. Photonics* **2011**, *5*, 738−743.
(16) Nikolajsen, T.; Leosson, K.; Bozhevolnyi, S. I. Surface Plasmon Polariton Based Modulators and Switches Operating at Telecom Wavelengths. *Appl. Phys. Lett.* **2004**, *85*, 5833−5835.
(17) Tang, L.; Kocabas, S. E.; Latif, S.; Okyay, A. K.; Ly-Gagnon, D.-S.; Saraswat, K. C.; Miller, D. A. B. Nanometre-Scale Germanium Photodetector Enhanced by a Near-Infrared Dipole Antenna. *Nat. Photonics* **2008**, *2*, 226−229.
(18) Neutens, P.; Van Dorpe, P.; De Vlaminck, I.; Lagae, L.; Borghs, G. Electrical Detection of Confined Gap Plasmons in Metal−Insulator−Metal Waveguides. *Nat. Photonics* **2009**, *3*, 283−286.
(19) Cai, W.; White, J. S.; Brongersma, M. L. Compact, High-Speed and Power-Efficient Electrooptic Plasmonic Modulators. *Nano Lett.* **2009**, *9*, 4403−4411.
(20) Ditlbacher, H.; Hohenau, A.; Wagner, D.; Kreibig, U.; Rogers, M.; Hofer, F.; Aussenegg, F. R.; Krenn, J. R. Silver Nanowires as Surface Plasmon Resonators. *Phys. Rev. Lett.* **2005**, *95*, 257403.
(21) Miyazaki, H. T.; Kurokawa, Y. Squeezing Visible Light Waves into a 3-nm-Thick and 55-nm-Long Plasmon Cavity. *Phys. Rev. Lett.* **2006**, *96*, 097401.
(22) Sorger, V. J.; Oulton, R. F.; Yao, J.; Bartal, G.; Zhang, X. Plasmonic Fabry-Pérot Nanocavity. *Nano Lett.* **2009**, *9*, 3489−3493.
(23) Cattoni, A.; Ghenuche, P.; Haghiri-Gosnet, A.-M.; Decanini, D.; Chen, J.; Pelouard, J.-L.; Collin, S. λ^3/1000 Plasmonic Nanocavities for Biosensing Fabricated by Soft UV Nanoimprint Lithography. *Nano Lett.* **2011**, *11*, 3557−3563.
(24) Bozhevolnyi, S. I.; Volkov, V. S.; Devaux, E.; Laluet, J.-Y.; Ebbesen, T. W. Channel Plasmon Subwavelength Waveguide Components Including Interferometers and Ring Resonators. *Nature* **2006**, *440*, 508−511.
(25) Min, B.; Ostby, E.; Sorger, V.; Ulin-Avila, E.; Yang, L.; Zhang, X.; Vahala, K. High-Q Surface- Plasmon-Polariton Whispering-Gallery Microcavity. *Nature* **2009**, *457*, 455−458.
(26) Vesseur, E. J. R.; García de Abajo, F. J.; Polman, A. Modal Decomposition of Surface-Plasmon Whispering Gallery Resonators. *Nano Lett.* **2009**, *9*, 3147−3150.
(27) Della Valle, G.; Søndergaard, T.; Bozhevolnyi, S. I. High-Q Plasmonic Resonators Based on Metal Split Nanocylinders. *Phys. Rev. B: Condens. Matter Mater. Phys.* **2009**, *80*, 235405.
(28) Xiao, Y.-F.; Li, B.-B.; Jiang, X.; Hu, X.; Li, Y.; Gong, Q. High Quality Factor, Small Mode Volume, Ring-Type Plasmonic Microresonator on a Silver Chip. *J. Phys. B: At., Mol., Opt. Phys.* **2010**, *43*, 035402.
(29) Kuttge, M.; Garcia de Abajo, F. J.; Polman, A. Ultrasmall Mode Volume Plasmonic Nanodisk Resonators. *Nano Lett.* **2010**, *10*, 1537−1541.
(30) Gong, Y.; Vuckovic, J. Design of Plasmon Cavities for Solid-State Cavity Quantum Electrodynamics Applications. *Appl. Phys. Lett.* **2007**, *90*, 033113.
(31) Weeber, J.-C.; Bouhelier, A.; Colas des Francs, G.; Markey, L.; Dereux, A. Submicrometer In-Plane Integrated Surface Plasmon Cavities. *Nano Lett.* **2007**, *7*, 1352−1359.
(32) Feng, L.; Lu, M.-H.; Lomakin, V.; Fainman, Y. Plasmonic Photonic Crystal with a Complete Band Gap for Surface Plasmon Polariton Waves. *Appl. Phys. Lett.* **2008**, *93*, 231105.
(33) Kim, M.-K.; Lee, S. H.; Choi, M.; Ahn, B.-H.; Park, N.; Lee, Y.-H.; Min, B. Low-Loss Surface-Plasmonic Nanobeam Cavities. *Opt. Express* **2010**, *18*, 11089−11096.
(34) Maksymov, I. S. Optical Switching and Logic Gates with Hybrid Plasmonic−Photonic Crystal Nanobeam Cavities. *Phys. Lett. A* **2011**, *375*, 918−921.
(35) Yang, X.; Liu, Y.; Oulton, R. F.; Yin, X.; Zhang, X. Optical Forces in Hybrid Plasmonic Waveguides. *Nano Lett.* **2011**, *11*, 321−328.
(36) Yang, X.; Ishikawa, A.; Yin, X.; Zhang, X. Hybrid Photonic-Plasmonic Crystal Nanocavities. *ACS Nano* **2011**, *5*, 2831−2838.
(37) Lakhani, A. M.; Kim, M.-k.; Lau, E. K.; Wu, M. C. Plasmonic Crystal Defect Nanolaser. *Opt. Express* **2011**, *19*, 18237−18245.
(38) Choo, H.; Kim, M.-K.; Staffaroni, M.; Seok, T. J.; Bokor, J.; Cabrini, S.; Schuck, P. J.; Wu, M. C.; Yablonovitch, E. Nanofocusing in a Metal-Insulator-Metal Gap Plasmon Waveguide with a Three-Dimensional Linear Taper. *Nat. Photonics* **2012**, *6*, 838−844.
(39) *Photonic Crystals: Molding the Flow of Light*, 2nd ed.; Princeton University Press: Princeton, 2008.
(40) Johnson, P. B.; Christy, R. W. Optical Constants of the Noble Metals. *Phys. Rev. B* **1972**, *6*, 4370.
(41) Purcell, E. M. Spontaneous Emission Probabilities at Radio Frequencies. *Phys. Rev.* **1946**, *69*, 674−674.
(42) Coccioli, R.; Boroditsky, M.; Kim, K. W.; Rahmat-Samii, Y.; Yablonovitch, E. Smallest Possible Electromagnetic Mode Volume in a Dielectric Cavity. *Optoelectron., IEE Proc.* **1998**, *145*, 391−397.